Three-Fold Coordination of Copper in Sulfides: A Blockade for Hole Carrier Delocalization but a Driving Force for Ultralow Thermal Conductivity

Krishnendu Maji, Bernard Raveau, P. Lemoine, Philippe Boullay, Paribesh Acharyya, Xingchen Shen, Adèle Renaud, Vincent Pelletier, Régis Gautier, Virginia Carnevali, et al.

Three-fold coordination of copper in sulfides: a blockade for hole carrier delocalization but a driving force for ultralow thermal conductivity

Krishnendu Maji,[1] Bernard Raveau,[1*] Pierric Lemoine,[2*] Philippe Boullay,[1] Paribesh Acharyya,[1] Xingchen Shen,[1] Adèle Renaud,[3] Vincent Pelletier,[3] Régis Gautier,[3] Virginia Carnevali,[4] Marco Fornari,[4] Bin Zhang,[5,6] Xiaoyuan Zhou,[5,6] Bertrand Lenoir,[2] Christophe Candolfi,[2] Emmanuel Guilmeau[1*]

[1]*CRISMAT, CNRS, Normandie Univ, ENSICAEN, UNICAEN, 14000 Caen, France*

[2]*Institut Jean Lamour, UMR 7198 CNRS – Université de Lorraine, 54011 Nancy, France*

[3]*Univ Rennes, Ecole Nationale Supérieure de Chimie de Rennes, CNRS, ISCR-UMR 6226, F-35000 Rennes, France*

[4]*Department of Physics and Science of Advanced Materials Program, Central Michigan University, Mt. Pleasant, MI 48859, USA*

[5]*College of Physics and Institute of Advanced Interdisciplinary Studies, Chongqing University, Chongqing 401331, China*

[6]*Analytical and Testing Center of Chongqing University, Chongqing 401331, China*

**Corresponding authors: emmanuel.guilmeau@ensicaen.fr, bernard.raveau@ensicaen.fr, pierric.lemoine@univ-lorraine.fr*

Abstract

Copper-rich sulfides are very promising for energy conversion applications due to their environment compatibility, cost effectiveness and earth abundance. Based on a comparative analysis of the structural and transport properties of Cu_3BiS_3 with those of tetrahedrite ($Cu_{12}Sb_4S_{13}$) and other Cu-rich sulfides, we highlight the role of the cationic coordination types and networks on the electrical and thermal properties. By precession-assisted 3D electron diffraction analysis, we find very high anisotropic thermal vibration of copper attributed to its threefold coordination, with anisotropic atomic displacement parameter up to 0.09 $Å^2$. Density functional theory calculations reveal that these Cu atoms are weakly bonded and give rise to low-energy Einstein-like vibrational modes that strongly scatter heat-carrying acoustic phonons, leading to ultralow thermal conductivity. Importantly, we demonstrate that the three-

fold coordination of copper in Cu_3BiS_3, and in other copper-rich sulfides constituted of interconnected CuS_3 networks, causes a hole blockade. This phenomenon hinders the possibility to optimize the carrier concentration and electronic properties through mixed valency Cu^+/Cu^{2+}, differently from tetrahedrite and most other copper-rich chalcogenides, where the main interconnected Cu-S network is built of CuS_4 tetrahedra. The comparison with various copper-rich sulfides demonstrates that seeking for frameworks characterized by the coexistence of tetrahedral and threefold coordinated copper is very attractive for the discovery of efficient thermoelectric copper-rich sulphides. Considering that lattice vibrations and carrier concentration are key factors for engineering transport phenomena (electronic, phonon, ionic…) in copper-rich chalcogenides for various types of applications, our findings improves the guidelines for the design of materials enabling sustainable energy solutions with wide-ranging applications.

Introduction

Over the past couple of decades, the generation of renewable and sustainable green energy has been at the centre of scientific attention due to the urgent need to reduce greenhouse gas emissions and global warming.[1] In order to tackle this issue, the scientific community must focus on finding more sustainable, renewable, and cost-efficient materials for energy conversion and storage. In this regard, the family of ternary and quaternary copper-based chalcogenides present a rich selection of potential candidates for Earth-abundant low-toxicity energy materials. They have shown highly promising prospects for many energy applications, such as thermoelectrics (TE), thin-film solar cells, dye-synthesised solar cells, photocatalysis, and batteries.[2–11]

Although copper-rich chalcogenides have been studied for several decades, the effects of the coordination types and the nature of crystal sub-lattices on both the electrical and thermal properties are still not fully understood. In this regard, *p*-type copper-rich sulfides for TE applications offer an attractive field of investigation to understand and clarify the effect of the nature of polyhedra and cationic networks on transport properties. The strategy is to find a route for developing, within the same matrix, two or more structural features which may enhance electron mobility and phonon scattering, concomitantly. Regarding electrical transport properties, most of copper-rich sulfides can be described as intrinsic or extrinsic (doped) degenerate semiconductors with metal-like conduction. This is in agreement with the concept

of "Cu(I)-Cu(II)" copper mixed valency,[12] which forms the basis of hole doping in TE Cu-based sulfides, with a high proportion of divalent copper being achievable. Note that, in those sulfides, the *p*-type metallic conductivity is due to charge delocalization in the tetrahedral Cu-S framework associated with the redox couple Cu^{2+}/Cu^{+}, but that Cu^{2+} does not occur as a static cation, contrary to CuS.[13]

Two interesting examples are tetrahedrites $Cu_{12-x}T_xSb_4S_{13}$ (T = Ni, Zn)[14–17] and colusites $Cu_{26}A_2E_6S_{32}$ (A = Ti, V, Cr, Nb, Mo, Ta, W; E = Ge, Sn, Sb) materials[18–22], which stand out for their TE performance— ZT approaching 1 around 700 K— because of their intrinsic degenerate semiconducting behavior and very low lattice thermal conductivity. However, the origin of low lattice thermal conductivity, κ_L, is very different in these two families. In colusites, the heat transport is mainly governed by the intrinsic structural complexity, which arises from the large sphalerite-derivative unit cells in which $[AS_4]Cu_6$ tetrahedral-octahedral complexes are present and functionalize the "Cu-S" conductive network.[18–20,22–24] Order/disorder phenomena are also known to enhance substantially phonon scattering, while keeping high power factors.[20,21,25] Differently, in tetrahedrites, copper exhibits two different types of coordination, tetrahedral and triangular, and low lattice thermal conductivity was shown to originate from high anisotropic atomic vibrations of copper in triangular coordination.[14,26–30]

Among all the thermoelectric copper-rich sulfides, the tetrahedrite family $Cu_{12-x}T_xSb_4S_{13}$ is, to the best of our knowledge, the only one that involves three-fold coordinated copper. In this respect, the recent synthesis of the copper-rich sulfide wittichenite Cu_3BiS_3 with low lattice thermal conductivity,[31–33] which was previously studied as thin films for photovoltaic absorbers,[34–36] appears as a very interesting route for the investigation of structural features (coordinations, cationic networks) governing the electronic and thermal conductivity of these materials.

The present investigation on Cu_3BiS_3 clearly establishes that the threefold coordination of copper, and its strong anisotropic vibration, has a key role on the two antagonist factors, electrical and thermal conductivity, which govern the thermoelectric properties of the Cu-rich sulfides. We observe that all attempts to introduce hole carriers on the copper lattice by doping the Bi sites with divalent cations or by introducing vacancies on the copper sites are hindered due to the strong rattling of three-fold coordinated copper. In contrast, many other Cu-rich sulfides including tetrahedrites, in which tetrahedral coordination of copper forms a 2D or 3D corner-sharing framework, allows an adequate overlapping of the Cu-*3d* and S-*3p* orbitals for the delocalization of hole carriers in agreement with the Cu(I)-Cu(II) mixed valence, and thus

to finely tune the carrier concentration and electronic properties. By comparing the coordination forms and cationic networks encountered in Cu_3BiS_3, tetrahedrite $Cu_{12}Sb_4S_{13}$ and other state-of-the-art Cu-based sulfides (**Figure 1**), we also point to the three-fold coordination as the driving force for the appearance of ultra-low thermal conductivity. We also suggest that the Bi^{3+} cation, due to its $6s^2$ electronic lone pair (LP) which forms a weak LP-Cu bond with the nearest Cu^+ cation, limits its large displacement with respect to the "S_3" plane, compared to low chalcocite Cu_2S. Our investigation demonstrates that the copper coordination is key for engineering and controlling electrical and thermal properties in copper-rich chalcogenides. These findings can have wide-ranging implications for the design of materials for energy technologies (photovoltaics, optics, thermoelectrics, batteries…), for which copper-rich chalcogenides are promising for their diverse functional properties.

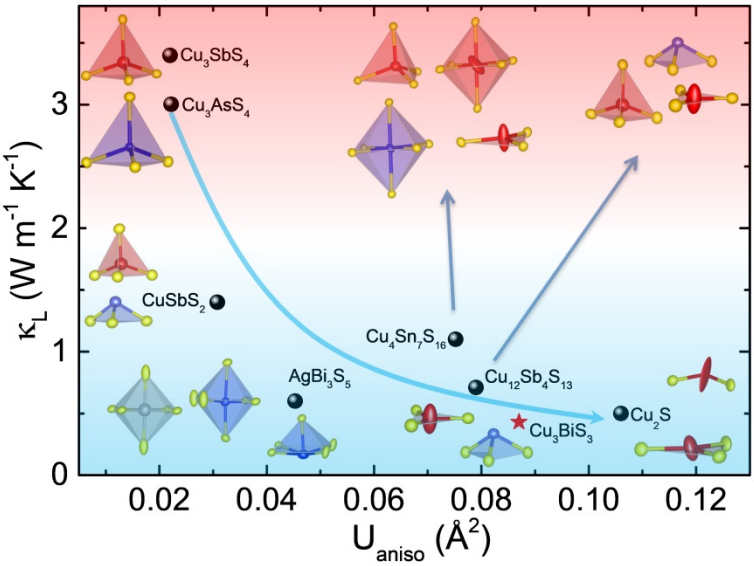

Figure 1. Plot of lattice thermal conductivity (κ_L) vs. maximum anisotropic atomic displacement parameter (U_{aniso}) of Cu atoms (except for Ag in $AgBi_3S_5$) of state-of-the-art Cu-based sulfides with the cationic coordination environment.[37–47] Plot of κ_L vs. U_{iso} is represented in **Figure S1**.

Results and Discussion

Structural analysis

The X-ray powder diffraction (XRPD) pattern of pristine Cu_3BiS_3 after spark plasma sintering (SPS), recorded at room temperature (RT), is indexed with an orthorhombic unit cell of space group $P2_12_12_1$ exhibiting refined unit cell parameters a = 7.6642(2) Å, b = 10.4202(3) Å, and

c = 6.7044(2) Å. High quality Rietveld refinement (**Figure 2a**) is obtained by considering the structural model of wittichenite, Cu_3BiS_3, published by Kocman and Nuffield,[48] where Cu, Bi and S atoms are located on three, one and three different 4a sites of general multiplicity, respectively. Moreover, the absence of non-indexed diffraction peaks suggests the formation of high purity Cu_3BiS_3 sample after SPS. The refined cell parameters and atomic coordinates of pristine sample are given in **Table S1**. To broaden the scope of the structural analysis, precession-assisted 3D electron diffraction (3D ED) measurements have been performed on four crystallites of the polycrystalline bulk sample, which present good reproducibility. Note that 3D ED is the only single-crystal diffraction method that can be used to study grains smaller than 200nm, as in our sample. The aim here is to obtain a more local approach to the crystalline structure of our sample, complementary to what is accessible by X-ray powder diffraction. The structural data determined from one 3D ED measurement are reported in **Table 1** and **Table S4**, and the corresponding bond distances and bond angles are gathered in **Table S5**. These results also confirm the structural model published by Kocman and Nuffield[48] and are in excellent agreement with the bond distances and bond angles determined from Rietveld refinement of the XRPD pattern.

In Cu_3BiS_3, Bi is three-fold coordinated by S (CN = 3, **Figure 2d**). Bi-S distances (see **Table S3** for XRPD and **Table S5** for 3D ED) ranging from 2.567 / 2.568 Å to 2.614 / 2.612 Å (XRPD / 3D ED) and S-Bi-S angles from 95.44° / 94.53° to 96.62° / 98.65°, lead to an average Bi-S distance ($\overline{d_{Bi-S}}$) of 2.584 / 2.59 Å (XRPD / 3D ED) and an average S-Bi-S angle ($\overline{\alpha_{S-Bi-S}}$) of 96.00° / 95.92° (XRPD / 3D ED). These values are in fair agreement with those encountered in $CuBiS_2$ (**Table S3**), a ternary Cu-based sulfide involving Bi^{3+} with a similar environment of sulfur[49] and indicate that the local environment of Bi in Cu_3BiS_3 is intermediate between triangular and tetrahedral coordination. Note that Kocman and Nuffield[48] reported an electron density excess in the proximity of the Bi atoms, which is most probably related to the $6s^2$ lone pair of Bi^{3+}. Hence, in wittichenite, the coordination environment of Bi should be viewed as a strongly distorted tetrahedron BiS_3LP where one apex is occupied by the $6s^2$ electronic lone pair of Bi^{3+}. This structural feature is observed in other ternary Cu-based sulfides involving a group VA element (noted *M*) with an electron lone pair (i.e. As^{3+}, Sb^{3+}, Bi^{3+}), and for which the Cu/*M* ratio is equal or higher than 1, such as in sinnerite $Cu_6As_4S_9$,[50] tennantite $Cu_{12}As_4S_{13}$,[51,52] tetrahedrite $Cu_{12}Sb_4S_{13}$,[27,53] skinnerite Cu_3SbS_3,[54,55] chalcostibite $CuSbS_2$,[56,57] and emplectite $CuBiS_2$[49] (**Table S3**).

In Cu_3BiS_3, all Cu atoms are in nearly trigonal planar coordination with S (CN = 3, **Figure 2b, c**), characterized by Cu-S distances ranging from 2.211 / 2.218 to 2.330 / 2.385 Å (XRPD / 3D

ED) and S-Cu-S angles ranging from 109.97° / 110.4° to 132.85° / 130.9° (XRPD / 3D ED). This leads to an average Cu-S distance ($\overline{d_{Cu-S}}$) of 2.274 / 2.288 Å (XRPD / 3D ED) and an average S-Cu-S angle ($\overline{\alpha_{S-Cu-S}}$) of 119.64° / 119.7° (XRPD / 3D ED), equivalent to those found for the Cu atoms in triangular coordination (CN = 3) of sulfur in $Cu_4Bi_4S_9$ (**Table S3**), another ternary Cu-based sulfide involving Bi^{3+} cations.[58,59] Such type of Cu triangular planar coordination can also be observed in few ternary Cu-based sulfides involving a group VA element with a LP, and Cu/*M* ratio ≥ 1, such as in tennantite ($Cu_{12}As_4S_{13}$),[51,52] tetrahedrite ($Cu_{12}Sb_4S_{13}$)[27,53] and skinnerite (Cu_3SbS_3),[54,55] (**Table S3**). Some of these phases exhibit intrinsically low lattice thermal conductivity due to LPs associated with elements of the group VA and to large anisotropic ADP for Cu atoms[55,58,60–62] (See discussion on the thermal properties in the last paragraph).

Estimation of the ADP parameters for Cu_3BiS_3 was only possible on the basis of 3D ED data (**Table 1**), which highlight large anisotropic ADP parameters for Cu atoms, particularly Cu(2), as illustrated in **Figure 3a, 3b and 3c**. This particularity is in agreement with the structure reported by Kocman and Nuffield using single-crystal X-ray diffraction analysis.[48] As shown in Figure 1 (see references in the caption), large anisotropic ADP values are commonly reported for Cu in triangular coordination, such as in tetrahedrite $Cu_{12}Sb_4S_{13}$, chalcocite Cu_2S, and $Cu_4Sn_7S_{16}$. Such large values, attributed from crystal chemistry and modelisation considerations to thermal motion of atoms (see below) in Cu_3BiS_3, might also reflect presence of static disorder such as atomic site splitting as exemplified in clathrate $Sr_8Ga_{16}Ge_{30}$,[63] Mo-based cluster $Ag_2Tl_2Mo_9Se_{11}$[64] or $Cu_4Sn_7S_{16}$.[65,66] Note that temperature dependence diffraction combined with inelastic neutron scattering experiments are currently on going in order to elucidate which parameter is mainly responsible of the large anisotropic ADP values in Cu_3BiS_3 and will be the scope of another publication.

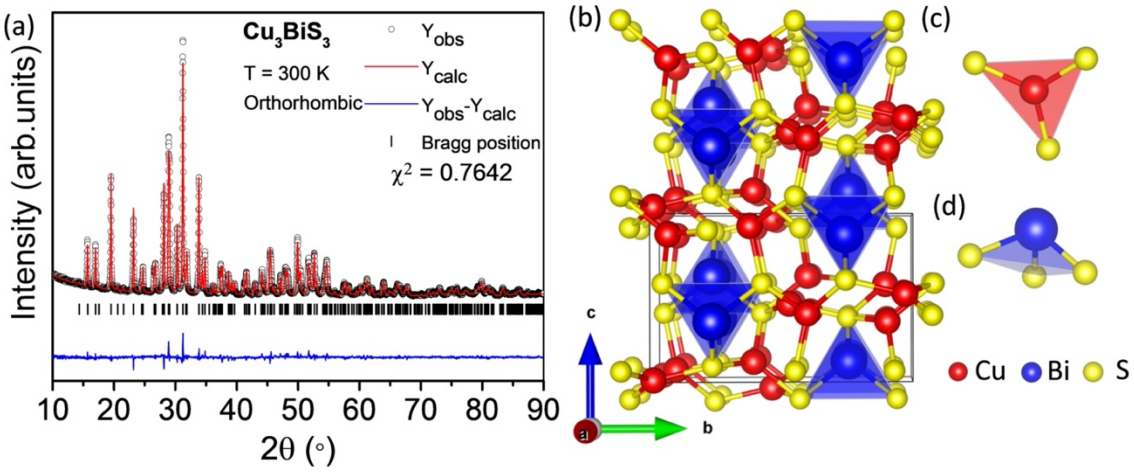

Figure 2. (a) Rietveld refinement of the XRPD data recorded at RT for Cu_3BiS_3 sample (λ = 1.5406 Å) and representations of the (b) orthorhombic crystal structure of Cu_3BiS_3 (space group – $P2_12_12_1$), (c) triangular planar environment of Cu atoms and (d) pyramidal coordination environment of Bi atoms.

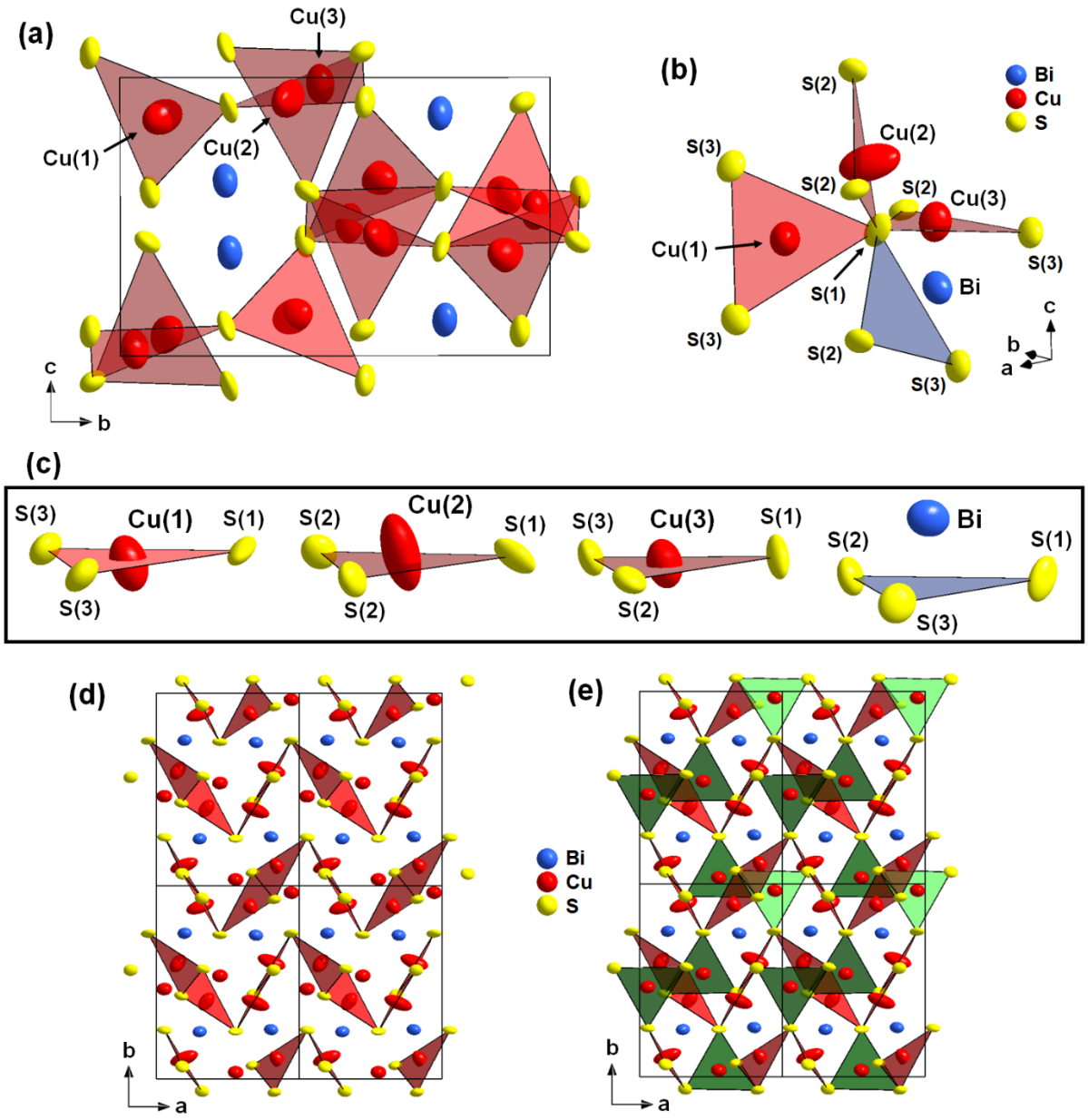

Figure 3. Crystal structure representations of Cu_3BiS_3 highlighting the large anisotropic displacements of Cu atoms in (a) the unit cell, (b) the polyhedron connection around the S(1) atom, and (c) the triangular configuration of Cu atoms and tetrahedral BiS_3LP configuration of Bi atom. Displacement ellipsoids are shown at the 90% probability level. Three-dimensional "Cu_3S_3" framework of Cu_3BiS_3: (d) Infinite corrugated layers of corner-sharing three-fold coordinated copper Cu(1) and Cu(2) parallel to (010) plane(red colored triangles) interleaved with bismuth layers (blue colored atoms), (e) Introduction of the three-fold Cu(3) (green colored triangles) to form the 3D "Cu_3S_3" framework.

Note that *Ab initio* molecular dynamics (AIMD) simulations are in very good agreement with the structural analysis. The Bi−S and Cu-S radial pair distribution functions (RDFs) obtained from NVT AIMD show a first peak centred on the experimental bond length ranges (**Figure S4**). The RDFs also indicate pronounced mobility for all atoms in the structure around their equilibrium positions. Indeed, the highest order peaks in the RDF fade rapidly as temperature increases.

It is important to analyze the structural behavior of Cu and Bi separately for properly characterizing the relationships between the structure and the electrical/thermal properties of this sulfide. Cu_3BiS_3 exhibits a $[Cu_3S_3]$ three-dimensional framework built up of corner-sharing triangular CuS_3 groups (**Figure 3d, e**). Two copper atoms (labelled Cu(1) and Cu(2)) form infinite corrugated layers (**Figure 3d**) of corner-sharing CuS_3 groups parallel to (010) plane. In those layers, each S atom is shared between two Cu^+ cations. The Cu(1)/Cu(2) layers are interleaved with Bi^{3+} layers whose $6s^2$ LP is probably alternately up and down oriented. Note that each copper cation belonging to these layers is sandwiched between two bismuth cations of the two adjacent bismuth layers, forming interatomic Bi···Cu···Bi distances of about 3.8 Å. Bearing in mind that the $6s^2$ Bi^{3+} lone pair may behave as an anion, the existence of $LP^{-\delta}\cdots Cu^{+}\cdots LP^{-\delta}$ interactions with distances of about 2.7 Å is most probable. Thus, this geometry explains the anisotropic rattling of the copper cations along the direction perpendicular to the S_3 plane inside a LPS_3LP cage, akin to a strongly distorted trigonal bipyramid. The third copper atom, labeled Cu(3) ensures the connection between two copper layers, sharing two of its apices with the same layer and the third one with the next layer (**Figure 3e**). As already discussed, the bismuth cations are three-fold coordinated to sulfur, forming a tetrahedron BiS_3LP with their $6s^2$ LP, and they are isolated from the other atoms in the structure. Finally, it is worth pointing out that the crystal structure consists of infinite Cu_3BiS_3 chains parallel to [001] which are linked by Cu-S bonds to form continuous sheets perpendicular to [010], as previously described by Kocman and Nuffield.[48] The short distances, ranging from 2.61 and 2.74 Å, connect Cu(1) and Cu(3) atoms, making infinite chains along the *c* direction. Cu(2) atoms are further away from other Cu atoms; the shortest Cu(2)-Cu distance is equal to ca. 3 Å.

Table 1. Anisotropic atomic displacement parameters (in $Å^2$) of atoms in Cu_3BiS_3 from 3D ED

Atom	U11	U22	U33	U12	U13	U23
Bi(1)	0.0235(7)	0.0147(7)	0.0277(6)	0.0011(6)	0.0037(6)	0.0009(8)
Cu(1)	0.032(2)	0.038(2)	0.0305(18)	0.0128(15)	0.0033(17)	0.0057(19)

Cu(2)	0.089(4)	0.030(2)	0.035(2)	0.025(2)	0.007(2)	0.0066(19)
Cu(3)	0.0292(19)	0.019(2)	0.038(2)	0.0007(14)	0.0027(15)	-0.0016(16)
S(1)	0.026(2)	0.008(2)	0.022(2)	0.001(2)	-0.0105(17)	-0.005(3)
S(2)	0.024(3)	0.016(3)	0.012(2)	0.001(2)	-0.0004(19)	-0.0042(19)
S(3)	0.023(3)	0.010(3)	0.025(3)	0.0024(19)	-0.002(2)	-0.002(2)

The structural, microstructural, and chemical analyses of the pristine Cu_3BiS_3 sample were also performed by scanning and transition electron microscopy (SEM and TEM, respectively). As shown in **Figure S5a** from low-magnification TEM image, pristine Cu_3BiS_3 sample exhibits quite small and isotropic grains with typical sizes ranging between few tens of nanometres to 200 nm. Such small grain size is typically observed in samples prepared by mechanical-alloying followed by SPS treatment.[39,67,68] High resolution TEM (HRTEM) images obtained along two different directions through tilting series on the same grain are depicted in **Figure S5c and S5d**. These two HRTEM images, and related diffraction patterns (insets) can be assigned respectively to the [111] and $[\bar{2}5\bar{1}]$ zone axes of the orthorhombic Cu_3BiS_3 phase, in agreement with the above structural results. EDX mapping shows large zones with homogenous distribution of Cu, Bi, and S atoms (**Figure S5b**).

SEM images of a fractured surface indicate a non-uniform grain size and fine microstructure (as shown in **Figure S6a** and **S6b**), as observed by TEM. Observations on polished surfaces (**Figure S6c and S6d**) confirms a good sample homogeneity and the presence of few secondary phase particles, with light mass probably corresponding $Cu_{2-\delta}S$ (as shown in round red circle and confirmed by TEM-EDS analyses (**Figure S7**)), which can be observed both in the fractured and polished surface (**Figure S6b** and **S6d**). Notably, this secondary phase was not detected by XRPD despite the high quality (*i.e.* large signal to noise ratio) of the data. Note that bubble-like nano cavities are observed in the SEM images and can be attributed to incomplete sintering and/or sulfur evaporation during SPS process. In general, this phenomenon can be found in sulfide-based materials, such as in aikinite-type compounds for instance.[67]

Electrical properties

The temperature dependence of the electrical resistivity (ρ) is shown in **Figure S8a**. The *ρ(T)* curve follows a non-degenerate semiconducting behavior with values decreasing from 130 Ω cm at 300 K to 0.36 Ω cm at 563 K. In the previous studies on Cu_3BiS_3, Wei *et al.* reported a comparable value of 140 Ω cm at RT while Adeyemi *et al.* measured an electrical resistivity value of 17.2 Ω cm at 318 K, i.e. one order of magnitude lower than our value.[31,32] This is mainly explained by the larger grain sizes (one order of magnitude larger) in the compounds synthesized by Adeyemi *et al*. The high electrical resistivity in our sample is consistent with its

high Seebeck coefficient S of 800 μV K^{-1} at RT (**Figure S8b**) and relatively low hole concentration of 1.7×10^{16} cm^{-3}. Those values attest of the relatively high purity and stoichiometry of our sample thanks to the synthesis approach which combines mechanical-alloying followed by SPS, preventing heavy sulfur loss and stoichiometric deviation.[67] Note that the phase formation of Cu_3BiS_3 is extremely fast (less than 30 min, **Figure S2a**) during mechanical-alloying (as described in the experimental section), and the subsequent SPS treatment allows to quickly complete the reaction and crystallization at relatively low sintering temperature.

All attempts to hole dope Cu_3BiS_3 using different dopants (aliovalent substitutions (Pb, Sn, Ag, Ca and Sr) and cationic vacancies) and synthesis techniques failed although the structure of Cu_3BiS_3, built up of a 3D framework of interconnected CuS_3 triangles, should favor an overlapping of the copper and sulfur orbitals and consequently hole delocalization. Nevertheless, a more detailed analysis of the structure shows the coexistence of two types of Cu-S bonds in the "Cu_3S_3" framework which may significantly affect the overlapping of the the Cu and S orbitals and consequently may prevent any hole delocalization. One indeed observes that this framework consists of Cu_3S_7 groups (**Figure 3b**), sharing the apices of their CuS_3 triangles. In those groups, the central sulfur atom (S1) is linked to three Cu^+ cations, while in the rest of the "Cu_3S_3" lattice, each S atom (S2, S3) is shared between two Cu^+ cations. The hole blockade most probably also originates from the large displacements of Cu^+, up to 0.3 Å from the center of the "S3" plane due to the strong rattling of the copper cations with respect to their three S neighbors. Consequently, the overlapping of the Cu and S orbitals is significantly weakened, hindering hole carrier exchange between two CuS_3 groups. This hypothesis is supported by the fact that the replacement of CuS_3 groups in the chalcocite by CuS_4 tetrahedra leading to the digenite $Cu_{1.96}S$ structure induces the formation of high carrier concentrations.[69] In a similar way, the metastable cubic form of Cu_3SbS_3 consisting of interconnected CuS_4 tetrahedra can also exhibit high carrier concentration of 10^{20} cm^{-3} by doping, in agreement with the fact that the majority of copper is in tetrahedral coordination and does not exhibit any abnormally high anisotropic vibration. In a more general way, we can affirm that all the Cu-rich sulfides, which exhibit a pure tetrahedral copper framework (i.e. group A phases with Cu/M ≥ 1 from copper-based sulfides classification)[70] are *p*-type conductors and can exhibit high hole carrier concentration by doping, as previously shown for $Cu_5Sn_2S_7$,[71] $Cu_{22}Sn_{10}S_{32}$,[72] Cu_3SbS_4,[73] Cu_2SnS_3[74] and $Cu_2(Fe,Zn)SnS_4$.[75,76] In other words, these results strongly suggest that the three-

fold coordination of copper is detrimental to the generation and delocalization of hole carriers in the Cu-rich sulfides, hindering the possibility to induce the mixed valency Cu(I)/Cu(II).

Additionally, DOS and COHP for main contacts were computed for Cu_3BiS_3; corresponding curves are sketched in **Figures 4a and S9**. Summing COHP values up to the Fermi level gives access to the contribution of a chemical bond to the distribution of one-particle energies and indicates the total bond strength. Those integrated COHP (ICOHP), averaged for Bi-S and Cu-S contacts are equal to -3.01 eV and -1.58 eV, respectively. It is noteworthy to mention that averaged ICOHP for shortest Cu-Cu and Bi-Cu contacts are equal to -0.22 and -0.16 eV, respectively. This demonstrates that bonding is weak but significant between copper and bismuth atoms in this structure. The width of the band gap computed within DFT at PBE exchange and correlation level is equal to 0.8 eV. An optical band gap close to this theoretical value, namely around 1.2 eV, was experimentally determined from diffuse reflectance measurements (**Figure 4b**). The bottom of the conduction band is dominated by Bi atoms and shows significant Bi-S and Cu-S antibonding character. The top of the valence band is mainly composed by copper orbitals and exhibit an antibonding Cu-S character. It is noteworthy to mention that these bands located at the top of the valence band are overall Bi-S and Cu-Cu nonbonding. Analysis of the electronic charge distribution and electron localization function (ELF) (**Figure 4c**) shows the presence of charge between Bi^{3+} and S^{2-}, highlighting the presence of directional covalent bonds between them, as well as that of a LP on the Bi^{3+} cations. In contrast, the distribution around the Cu^{+} cations in both charge and ELF contours is reasonably isotropic and spherical, showing that Cu^{+} has very weak electrostatic interaction with the environment, which support its rattling behavior. Owing to these calculations and assuming a rigid band model, oxidation and/or hole-doping of the title compound should strengthen the bonding in this structure. The electronic structures of several hypothetical compounds of general formula $Cu_3Bi_{2.75}M_{0.25}S_3$ (M = Ca, Cd, Pb, Sn, Sr) have been also studied (the theoretical DOS given in the Supporting Information section, **Figures S10 and S11**), Those results confirm the rigid band model, *i.e.* the electronic band structure is hardly affected by this doping, suggesting that such doping may not enhance the Seebeck coefficient. Such a hole blockade was also observed for monoclinic Cu_2S chalcocite whose 3D Cu-S framework is built of corner-sharing CuS_3 groups exclusively.[47,77] In the same way, the monoclinic or orthorhombic forms of the skinnerite (Cu_3SbS_3) which involve interconnected CuS_3 groups were found to exhibit a high electrical resistivity and no possibility of doping was reported so far for these compounds.[55,61]

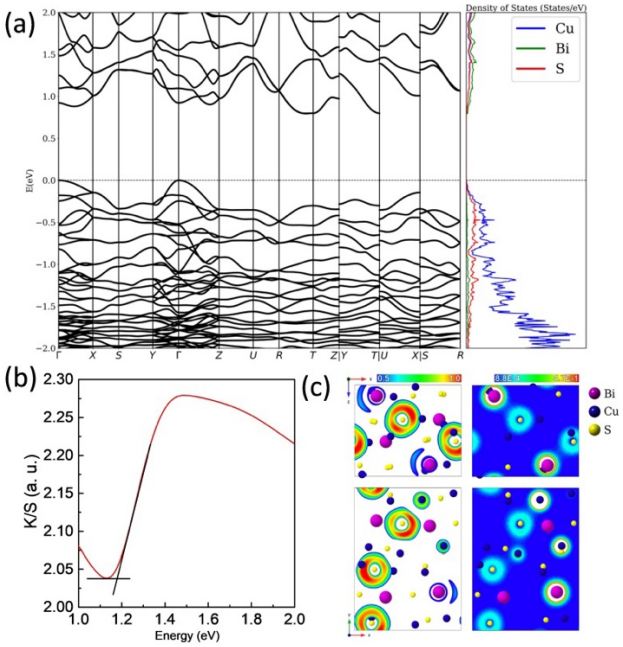

Figure 4. (a) Electronic bands structure (left panel) and atom-projected electron density of states (right panel) of Cu_3BiS_3. Spin−orbit coupling has been included in the calculation. Hubbard U corrections are included. The top of the valence band is set to 0 eV. (b) Kubelba-Munk transform obtained from the reflectance spectra and band gap determination taken at the intersection of the tangents at the absorption thresholds. (c) Contour of the ELF (left panel) and electron charge density (right panel) on the (010) (top) and (001) (bottom) planes. Values for the ELF range between 0 and 1: ELF = 0.5 (blue contour) indicates free electron behavior, and ELF = 1.0 (red contour) indicates perfect localization. Values smaller than 0.5 are less significant and usually point to small local electron densities. The scale bar for the electron charge density plot goes from 8.79×10^{-4} e/bohr^3 (blue contour) to 6.61×10^{-4} e/bohr^3 (red contour).

The temperature dependence of the power factor is displayed in **Figure S8c**. The maximum value is relatively low, *i.e.* around 0.45 μW cm^{-1} K^{-2} at 563K, which is due to the high electrical resistivity and low carrier concentration. This value is comparable to those reported in some non-degenerate semiconductors such as Cu_3SbS_4 (~1.26 μW cm^{-1} K^{-2} at 623 K),[73] Cu_2SnS_3 (0.2 μW cm^{-1} K^{-2}, 700 K),[74] and remains much lower than those of degenerate semiconductors $Cu_{22}Sn_{10}S_{32}$, (9.5 μW cm^{-1} K^{-2} at 700 K),[72] $Cu_5Sn_2S_7$ (~ 9.4 μW cm^{-1} K^{-2} at 700 K),[71] colusite $Cu_{26}V_2Sn_6S_{32}$ (7.0 μW cm^{-1} K^{-2} at 675 K)[21] and tetrahedrite $Cu_{12}Sb_4S_{13}$ (~11.9 μW cm^{-1} K^{-2} at 725 K),[78] due to their lower electrical resistivity (higher carrier concentration). Finally, the

reversibility of the electrical properties (electrical resistivity and Seebeck coefficient) of pristine Cu_3BiS_3 up to 563 K (five cycles from 345 K to 512 K + five cycles from 345 K to 563 K) indicates the thermal stability of the sample within the temperature range investigated (**Figure S12**).

The change of slope observed in the electrical resistivity and Seebeck coefficient around 375 K (**Figure S8a and S7b, S12a and S12b**) has been attributed to a structural phase transition in Cu_3BiS_3 occurring above room temperature. Indeed, a previous study by Makovicky[79] has highlighted that Cu_3BiS_3 phase exhibits a structural transition from a RT orthorhombic ($P2_12_12_1$) structure to an intermediate modulated structure at 391.5 K, and above 463 K, a transition to a high temperature (HT) polymorph ($Pnma$). Thermodynamic properties are also influenced by this structural phase transition as shown by the evolution of C_p within the temperature range of 325 K to 573 K (**Figure S13**). The abrupt change in C_p at around 373 K can be attributed to the phase transition from the RT to HT polymorph via an intermediate phase. This is also visible in the differential scanning calorimetry (DSC) study (**Figure S14**), which is comparable to the ones reported by Mizota *et al.*[80] Above 450 K, the HT polymorph phase is stabilized and the compound starts to decompose above 580 K (**Figure S14**).

Thermal Properties

The pristine phase Cu_3BiS_3 has an extremely low lattice thermal conductivity ($\kappa \approx \kappa_L$ due to the negligible electronic contribution) of 0.43 W m^{-1} K^{-1} at 300 K, which decreases as the temperature increases to reach 0.32 W m^{-1} K^{-1} at 563 K (**Figure 5a**). These values are slightly higher than those reported by Jia *et al*. (0.32 W m^{-1} K^{-1} at 300 K),[33] Adeyemi *et al.*[32] (0.29 W m^{-1} K^{-1} at 313 K) and Wei *et al.*[31] (0.17 W m^{-1} K^{-1} at 300 K). These differences could be the result of additional impurity phases and/or lower bulk sample density in these prior studies. It is also important to note that the samples synthesized by Adeyemi *et al*. exhibit grain sizes of several μms (200 nm in our sample) and densities of 93% (similar to our sample density) without any bubble-like cavities. So, it is unlikely that additional extrinsic effects suppress the lattice thermal conductivity in Cu_3BiS_3.

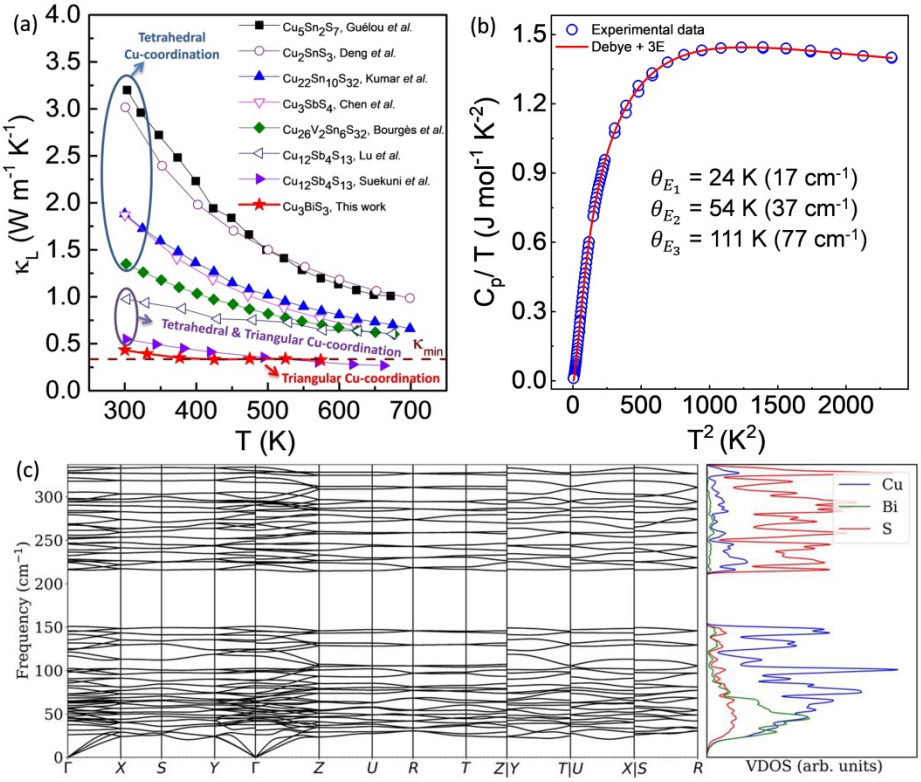

Figure 5. (a) Comparison of $\kappa_L(T)$ curves from state-of-the-art Cu-rich thermoelectric sulfides[14,17,21,72–74,81] with Cu_3BiS_3. (b) Debye–Einstein fit of C_p/T vs T^2 plot and (c) Phonon dispersions (left) and projected phonon density of states (PDOS) (right) of Cu_3BiS_3.

To further shed light on the ultralow κ_L values in Cu_3BiS_3, we have measured the low temperature specific heat (**Figure S15a**). We found that the plot C_p/T vs. T^2 could be well fitted using a combined Debye-Einstein model in the temperature range of 2-33 K (**Figure 5b**). The Debye model alone is not sufficient to fit the experimental data due to the presence of weakly-dispersive, low-energy optical phonon modes which correspond to independent or nearly independent atomic vibrations that can be typically modelled as Einstein oscillators. The Debye-Einstein model can be expressed by the following equation (1)[82]:

$$\frac{C_p}{T} = \gamma + \beta T^2 + \sum_n \left(A_n \left(\theta_{E_n}\right)^2 . (T^2)^{-3/2} . \frac{e^{\theta_{E_n}/T}}{\left(e^{\theta_{E_n}/T} - 1\right)^2} \right) \quad (1)$$

The coefficient of the first term in the equation is the Sommerfeld coefficient γ and represents the electronic contribution, and the coefficient of the second term, β, depicts the lattice contribution. The third term in the equation represents contributions from the Einstein oscillators corresponding to the localized vibrations where the A_n is the spectral weight and θ_{E_n}

is the Einstein temperature of the n^{th} Einstein oscillator mode. A good fit of the data could be achieved with three Einstein modes of θ_{E_1} = 24 K (17 cm^{-1}), θ_{E_2} = 54 K (37 cm^{-1}), and θ_{E_3} = 111 K (77 cm^{-1}) (**Figure 5b**, **Table S6**). These modes involve mainly the thermal vibrations of Cu^+ and Bi^{3+}, as evidence by *ab initio* calculations of the phonon dispersions and vibrational DOS of Cu_3BiS_3 (**Figure 5c**). The phonon spectrum shows features similar to those observed in other copper sulfides with low κ_L,[67,72,83] with notably a low-energy manifold of optical modes centered at about 30 cm^{-1}. It is also in good agreement with the recent data reported by Jia *et al*.[33] The data plotted as C_p/T^3 vs. T (**Figure S15b**) show the presence of a pronounced peak centred near 9 K, which originates from the excess phonon density of states induced by the localized, low-energy optical modes. The Debye temperature (Θ_D) inferred from this model, estimated using the relation $\beta = C(12\pi^4 N_A k_B/5) \cdot (\Theta_D)^{-3}$, is equal to 242 K. In eq.(1), C is defined as $C = 1 - \sum_n A_n/3NR$, (N is the number of atoms per formula unit and R = 8.314 J mol^{-1} K^{-1} is the universal gas constant), with N_A and k_B being the Avogadro's number and Boltzmann constant, respectively. The Debye temperature is comparable to the state-of-the-art low κ_L materials as shown in **Table S7**. The presence of these modes can substantially impact the propagation of acoustic phonons through a drastic suppression of their available phase space, thereby lowering κ_L. Furthermore, these modes can maintain three-phonon Umklapp scattering events to lower temperatures, suppressing the Umklapp peak in κ_L.

For further clarification, longitudinal and transverse sound velocities were measured at 300 K and the average sound velocity was calculated using **equation S1**. The low average sound velocity of 1932 m s^{-1} at 300 K, which is comparable to those of other ultralow κ_L chalcogenides (**Table S7**), is consistent with the presence of soft bonding interaction. Moreover, the large Grüneisen parameter γ of 1.93, estimated from the measured sound velocities (**equations S2 and S3**), is also comparable with other reported materials exhibiting ultralow κ_L (**Table S7**). In Cu_3BiS_3, κ_L reaches the minimum theoretical value of 0.33 W m^{-1} K^{-1} (**Figure 5a**), calculated from **equation S5**.[84] It is noteworthy to mention that the occupation of the *p-d** antibonding states (COHP calculation, **Figure 4** and **S9**) would naturally destabilize the Cu-S bond strength, due to the decrease of the bond order. The consequence of the weak bond is the low speed of sound and high phonon-phonon scattering rates, which contribute to low lattice thermal conductivity. The connection between antibonding character and thermal conductivity has well been described in few earlier reports.[85,86]

Intriguingly, κ_L shows less temperature dependency than predicted by the conventional T^{-1} law for Umklapp scattering, with κ_L values being essentially constant above 375 K (**Figure**

5a). Similarly, the chain-like compounds TlSe, $TlInTe_2$, Tl_3MX_4 (M = V, Nb, and Ta; X = S and Se), $AgBiTe_2$, $AgSbTe_2$, and $Cs_3Bi_2I_6Cl_3$ have all shown such departure from the usual law.[87–91] Theoretically, these deviations have been demonstrated to be a signature of intrinsic anharmonicity resulting in pronounced renormalization effects on the frequencies of optical phonon modes that shape the low-energy part of the vibrational spectrum of these materials. Further temperature-dependent inelastic neutron scattering experiments will be important to determine whether the low-energy optical modes in Cu_3BiS_3 soften upon cooling, as observed for instance in tetrahedrites and synonymous with a high degree of anharmonicity,[92] or if the Cu atoms shows large static disorder similar to what has been observed in the type-I clathrate $Sr_8Ga_{16}Ge_{30}$ for instance.[93]

Discussion

The comparison of the crystal structure and transport properties of Cu_3BiS_3 with those of other Cu-rich sulfides strongly suggests that the copper coordination plays a central role in determining the electronic and thermal properties of this compound. Cu-rich sulfides in which a pure tetrahedral coordination of copper is observed (i.e. group A phases from copper-based sulfides classification[70]: Cu_3SbS_4, Cu_2SnS_3, $Cu_5Sn_2S_7$, $Cu_{22}Sn_{10}S_{32}$ …), can be easily doped due to adequate overlapping of the Cu-*3d* and S-*3p* orbitals that favors the delocalization of hole carriers, leading to high electrical conductivity. This is in contrast with the extremely low electrical conductivity and hole blockade for hole carrier delocalization observed for Cu_3BiS_3, low chalcocite Cu_2S and skinnerite Cu_3SbS_3, all of them containing three-fold coordinated copper exclusively (i.e. group D or group E phases from copper-based sulfides classification[70]). In the same way, comparing the temperature dependence of κ_L of Cu_3BiS_3 with those of other Cu-rich thermoelectric sulfides (**Figure 5a**) evidences that the same structures composed of CuS_4 tetrahedra exclusively (Cu_3SbS_4, Cu_2SnS_3, $Cu_5Sn_2S_7$, $Cu_{22}Sn_{10}S_{32}$) have significantly larger κ_L compared to Cu_3BiS_3. This is illustrated by the famatinite Cu_3SbS_4, which exhibits an ordered sphalerite network leading to very weak anisotropic thermal displacement of cations (**Tables S9 and S10**, **Figure S16**). In this compound, all cations are in tetrahedral coordination with average bond angles $\overline{\alpha}$ values equal to 109.5° (**Table S11**) indicating sp^3 hybridization of valence electron orbitals in agreement with the formal charges Cu^+ and Sb^{5+}.

From the above considerations, it appears that the coexistence of three-fold coordinated and tetrahedral copper within the same crystal structure in controlled proportions is very attractive for the conciliation of the two antagonist factors, electrical and thermal conductivity, which

govern the thermoelectric properties of Cu-rich sulfides. In this respect, the thermoelectric tetrahedrite $Cu_{12}Sb_4S_{13}$ deserves a particular attention.[14–17] This sulfide exhibits an electrical conductivity similar to those of pure tetrahedral Cu-rich sulfides and a lattice thermal conductivity intermediate between those of pure tetrahedral and pure three-fold Cu_3BiS_3 sulfides (**Figure 5a**), leading to attractive thermoelectric characteristics. The analysis of its crystal structure shows that the $Cu_{12}S_{13}$ network consists of two copper sub-lattices, labelled Cu(1) and Cu(2), formed by an equal number of copper cations (**Figures 6a and 6b**). The Cu(1) sub-lattice framework is built up by corner-sharing $Cu(1)S(1)_4$ tetrahedra and can be described as a copper-deficient sphalerite "$Cu_6\square_6S_{12}$" structure with large intersecting tunnels running along the <110> and the <111> directions (**Figures 6c and 6d**). Due to its similarity with the sphalerite derivatives, the geometry of this tetrahedral framework allows a perfect overlapping of the Cu(1)-*3d* and S(1)-*3p* orbitals, which explains the high electrical conductivity of this material and its doping ability. One indeed observes for this framework very small anisotropic thermal displacements parameters of Cu(1) atoms and longer interatomic distances (**Tables S12** and **S13**), similar to those observed in Cu_3SbS_4 (**Tables S9**and **S10**).

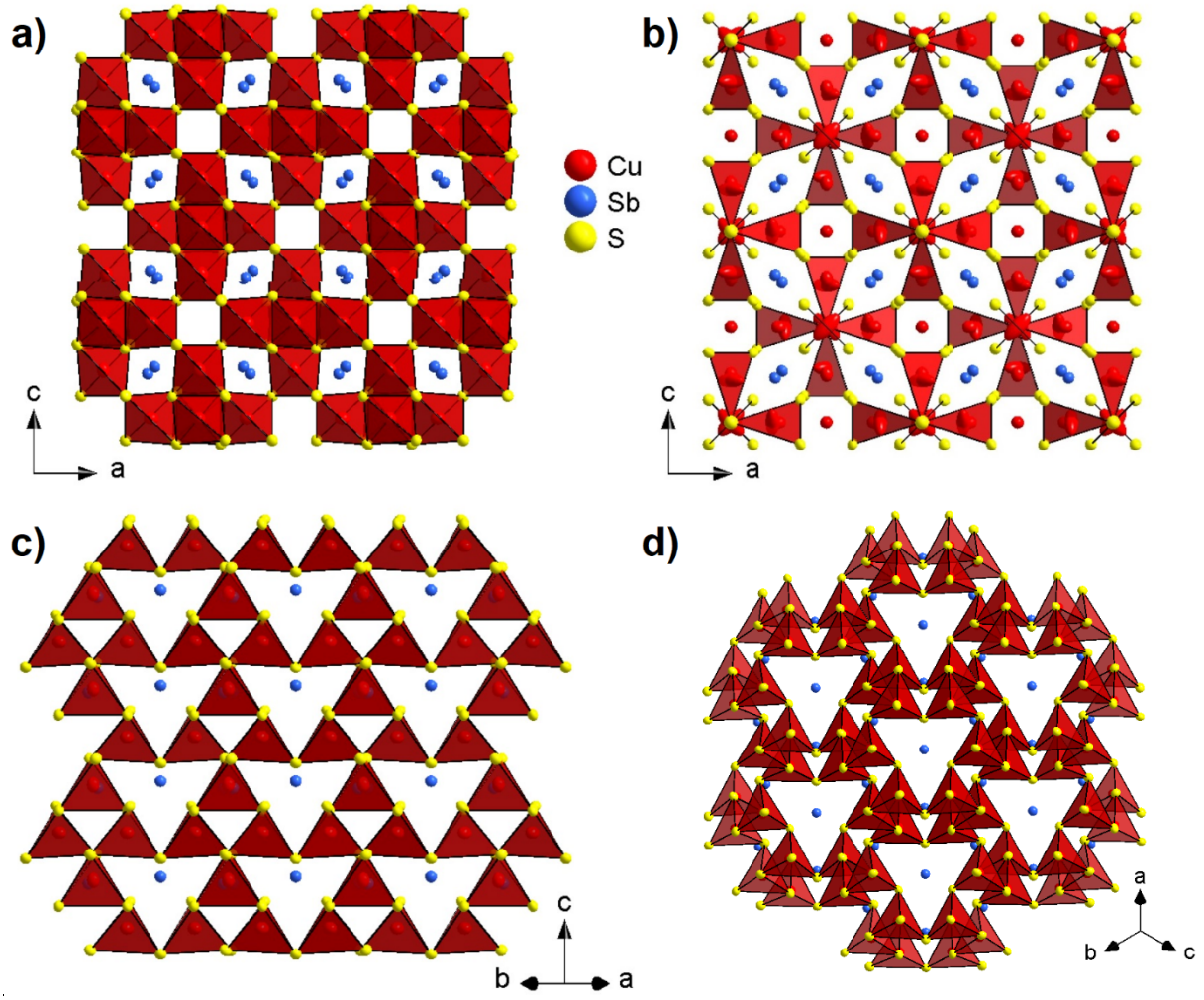

Figure 6. (a) and (b) crystal structure representation along the [010] direction of the Cu(1) and Cu(2) sub-lattice frameworks, respectively, highlighting the tetrahedral coordination of Cu(1) atoms and the three-fold coordination of Cu(2) atoms in tetrahedrite $Cu_{12}Sb_4S_{13}$. (c) and (d) crystal structure representation of the copper-deficient sphalerite "$Cu_6\square_6S_{12}$" framework (i.e. Cu(1) sub-lattice framework) in tetrahedrite $Cu_{12}Sb_4S_{13}$ along the [110] and [111] direction, respectively, highlighting large triangular tunnels along these directions where are located Sb, Cu(2) and S(2) atoms. For sake of clarity, atoms Cu(2) and S(2) were not represented in (a), (c), and (d). Displacement ellipsoids are shown at the 90% probability level.

As in Cu_3BiS_3, the Cu(2) cations in $Cu_{12}Sb_4S_{13}$ exhibit a three-fold coordination. However, the $Cu(2)S_3$ groups do not give rise to a 2D or 3D framework by sharing their apices but form isolated Cu_6S_{13} units whose central S(2) atom is shared between six $Cu(2)S(1)_2S(2)$ groups (**Figures 6b, 7a and 7b**). The Cu_6S_{13} units are in the <111> tunnels of the copper-deficient sphalerite "$Cu_6\square_6S_{12}$" framework (**Figures 6c and 6d**) and form columns along this direction (**Figure 7c**). Note that the Cu_6S_{13} units, formed exclusively of Cu(2) cations, share the 12 S(1)

apices of their $Cu(2)S(1)_2S(2)$ groups with the $Cu(1)S(1)_4$ tetrahedra of the "$Cu_6\square_6S_{12}$" framework. As a consequence, the anisotropic rattling of copper cations perpendicular to the "S_3" plane is limited to the Cu(2) atoms located inside of the <111> triangular columns of the copper-deficient sphalerite "$Cu(1)_6\square_6S_{12}$" framework (**Figure 7d**). Similar to Cu_3BiS_3 (**Table 1**), a large anisotropic ADP is observed for Cu(2) position in the perpendicular direction of the triangular plane with Cu(2)-S interatomic distances shorter than Cu(1)-S ones (**Tables S12** and **S13**). Nevertheless, in contrast to Cu_3BiS_3, the copper rattling is not extended over all the 3D frameworks. Hence, the influence of the crystal structure of tetrahedrite $Cu_{12}Sb_4S_{13}$ on the lattice thermal conductivity can be viewed as intermediate between that of famatinite Cu_3SbS_4 and that of wittichenite Cu_3BiS_3.

Moreover, as in Cu_3BiS_3, $Cu_{12}Sb_4S_{13}$ contains a lone pair of electrons with the $5s^2$ electron configuration of Sb^{3+}, leading to a tetrahedral SbS_3LP coordination. This cation is sandwiched between two Cu_6S_{13} units (**Figure 7c**), and consequently, may also influence the rattling of copper along the <111> directions, as suggested by the orientation of the main axis of Cu atoms ellipsoids directed toward the vacant apex of the pseudo-tetrahedron where the lone pair electrons is expected to be localized (**Figure 7b**). Nevertheless, contrary to state-of-the-art "lone-pair compounds",[94–97] the Bi^{3+} $6s^2$ LP in Cu_3BiS_3 cannot be considered itself as significantly responsible for the extremely low thermal conductivity in Cu_3BiS_3. Indeed, according to Skoug *et al.*[98], the average bond angles $\bar{\alpha}$ value of Bi in Cu_3BiS_3 (96.00° from XRPD and 95.92° from 3D ED, CN = 3) should lead to a lattice thermal conductivity value much higher than that determined experimentally (i.e. between 1.0-1.5 instead of 0.43 W m^{-1} K^{-1}, according to Skoug *et al.*[98]) (**Figure S18**)

Finally, it is worth pointing out that the presence of a LP cation is not necessary to induce a three-fold coordination of copper. This is illustrated in the low chalcocite Cu_2S structure (space group $P2_1/c$)[47] containing CuS_3 groups exclusively, and showing in a similar way, large anisotropic atomic displacement parameter for Cu. Importantly, the values of lattice thermal conductivity of 0.43-0.29 W m^{-1} K^{-1}, observed by Tang *et al.* in the temperature range of 300-380 K[46] for this compound, also strongly support our above statement that the presence of a LP cation such as Bi^{3+} or Sb^{3+} is not a necessary condition for the appearance of ultralow thermal conductivity in those Cu-rich sulfides. Nevertheless, a full understanding of the correlation between lattice dynamics, static disorder, and thermal conductivity in Cu_3BiS_3 will require further experimental and theoretical investigations.

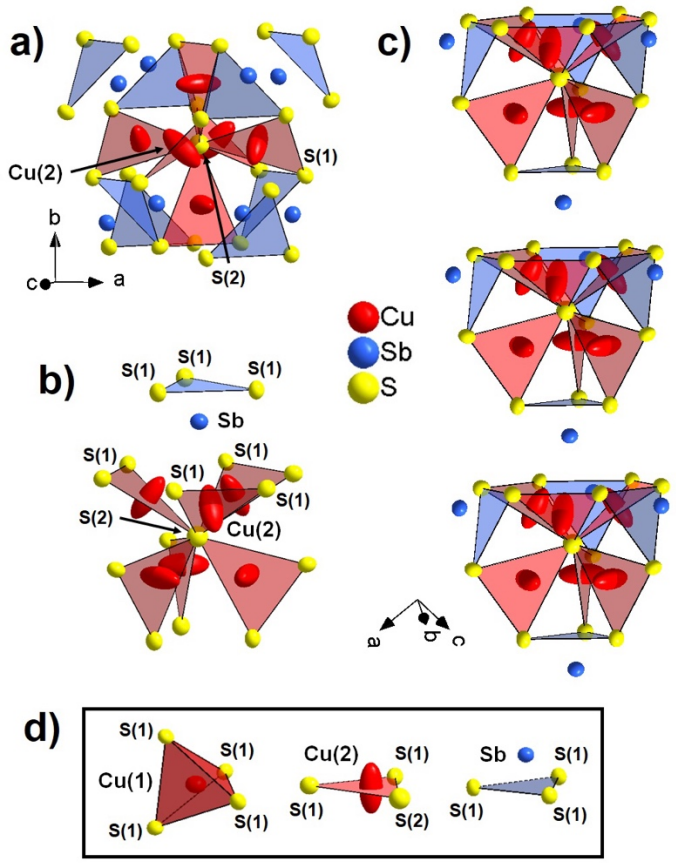

Figure 7. Representation in tetrahedrite $Cu_{12}Sb_4S_{13}$ of (a) the Cu_6S_{13} unit formed of six $Cu(2)S(1)_2S(2)$ groups sharing only the central S(2) atom and surrounded by eight SbS_3LP tetrahedra, (b) the Cu_6S_{13} unit highlighting the large anisotropic displacements of Cu(2) atoms perpendicularly to the $S(1)_2S(2)$ triangular plane and pointing to the vacant apex of Sb^{3+} pseudo-tetrahedron where the lone pair of electrons is expected to be localized, (c) alternatively stacking of Cu_6S_{13} units with SbS_3LP tetrahedra along the [111] direction highlighting the isolated nature of the Cu_6S_{13} units, and (d) the highly isotropic displacements of Cu(1) and Sb cations in (pseudo-)tetrahedral coordination and the large anisotropic displacement of Cu(2) in three-fold coordination. Displacement ellipsoids are shown at the 90% probability level.

Conclusion

The present detailed study of Cu_3BiS_3 and the comparison with the tetrahedrite $Cu_{12}Sb_4S_{13}$ and other copper-rich sulfides clearly show that the copper coordination is a key factor for engineering the transport properties and optimizing the thermoelectric properties. The extremely low electrical conductivity of this sulfide, as well as those of the low chalcocite Cu_2S and skinnerite Cu_3SbS_3, and their blockade for hole carrier delocalization, originate from the

three-fold coordination of copper. This is in contrast with many other Cu-rich sulfides, whose tetrahedral coordination of copper, forming a 2D or 3D corner-sharing framework, allows an adequate overlapping of the Cu-*3d* and S-*3p* orbitals for the delocalization of hole carriers in agreement with the Cu(I)-Cu(II) mixed valence, enabling to accurately tune the carrier concentration and electronic properties. In contrast, the three-fold coordination of copper favors anisotropic thermal vibrations that are associated with low-energy optical phonon modes, and, consequently, is a trump for the appearance of ultra-low thermal conductivity. Importantly, the presence of cations with LPs, such as Bi^{3+} or Sb^{3+} appears as a crucial factor for the stabilisation of the structure, and the proximity of this electronic LP, acting as an anion, with respect to three-fold coordinated Cu^{+}, may modulate the intrinsic thermal vibrations of Cu for optimizing the thermal conductivity. In conclusion, the realization of mixed frameworks involving the coexistence of two different types of polyhedra for copper (three-fold and tetrahedra) within the same matrix is a very attractive line of research to pursue for the discovery of efficient thermoelectric copper-based chalcogenides. This specific feature, described in high *ZT* tetrahedrite $Cu_{12}Sb_4S_{13}$, has been recently reported in Cu_2ZrS_3, a 2D structure without LP cation, and exhibiting extremely low lattice thermal conductivity.[99] Considering that copper-rich sulfides are also widely investigated for various applications and that thermal, electrical, but also mechanical and ionic properties of solids are closely related to atomic displacements and/or carrier concentration, we expect our findings to have wide materials-development implications.

Supporting Information

Supplemental information can be found online at

A details of experimental and theoretical methods, Figures S1-S18 and Table S1-S17, including κ_L *vs* $U_{iso,}$ XRPD, electrical and thermal trasport, radial distribution function (RDFs), average COHP, DOS, cycling measurement of electrical trasport, Cp *vs* T, DSC, TGA, κ_L *vs* bond angle plot, HRTEM, EDX, SEM data, crystal structure, refinement cell parameters after PAED, parameter after low temperature C_p fitting, claculated average sound velocity, Grüneisen parameter, Debye temperature from measured sound velocity and anisotropic atomic displacement parameters of atoms from SCXRD data.

Author Contributions

The manuscript was written through contributions of all authors. All authors have given approval to the final version of the manuscript.

Funding

PA and EG acknowledge Region Normandy under the program « RIN Recherche Emergent » (n°22E02729) for financial support. XS and EG acknowledges funding from the European Union's Horizon 2020 research and innovation program under the Marie Sklodowska- Curie grant agreement No. 101034329, and the WINNING- Normandy Program supported by the Normandy Region.

Acknowledgements

The authors gratefully thank Christelle Bilot and Jerôme Lecourt for technical support. PL acknowleges the X-ray diffraction centre of Institut des Sciences Chimiques de Rennes. Calculations were performed at the High-Performance Computing Center at Michigan State University.

Declaration of Interest

The authors declare no competing interests.

REFERENCES

(1) Rintoul, S. R.; Chown, S. L.; DeConto, R. M.; England, M. H.; Fricker, H. A.; Masson-Delmotte, V.; Naish, T. R.; Siegert, M. J.; Xavier, J. C. Author Correction: Choosing the Future of Antarctica. *Nature* **2018**, *562* (7726), 233–241. https://doi.org/10.1038/s41586-018-0369-7.

(2) Chen, S.; Walsh, A.; Gong, X. G.; Wei, S. H. Classification of Lattice Defects in the Kesterite Cu_2ZnSnS_4 and $Cu_2ZnSnSe_4$ Earth-Abundant Solar Cell Absorbers. *Adv. Mater.* **2013**, *25* (11), 1522–1539. https://doi.org/10.1002/adma.201203146.

(3) Kush, P.; Deka, S. Multifunctional Copper-Based Quaternary Chalcogenide Semiconductors Toward State-of-the-Art Energy Applications. *ChemNanoMat* **2019**, *5* (4), 373–402. https://doi.org/10.1002/cnma.201800321.

(4) Lokhande, A. C.; Babar, P. T.; Karade, V. C.; Gang, M. G.; Lokhande, V. C.;

Lokhande, C. D.; Kim, J. H. The Versatility of Copper Tin Sulfide. *J. Mater. Chem. A* **2019**, *7* (29), 17118–17182. https://doi.org/10.1039/c9ta00867e.

(5) Le Donne, A.; Trifiletti, V.; Binetti, S. New Earth-Abundant Thin Film Solar Cells Based on Chalcogenides. *Front. Chem.* **2019**, *7*, 297. https://doi.org/10.3389/fchem.2019.00297.

(6) Olatunde, O. C.; Onwudiwe, D. C. Stoichiometric Phases and Mechanism of Crystal Phase Selectivity of Copper-Based Ternary Sulphides. *Mater. Sci. Semicond. Process.* **2021**, *125*, 105627. https://doi.org/10.1016/j.mssp.2020.105627.

(7) Lokhande, A. C.; Chalapathy, R. B. V.; He, M.; Jo, E.; Gang, M.; Pawar, S. A.; Lokhande, C. D.; Kim, J. H. Development of Cu_2SnS_3 (CTS) Thin Film Solar Cells by Physical Techniques: A Status Review. *Sol. Energy Mater. Sol. Cells* **2016**, *153*, 84–107. https://doi.org/10.1016/j.solmat.2016.04.003.

(8) Peccerillo, E.; Durose, K. Copper—Antimony and Copper—Bismuth Chalcogenides—Research Opportunities and Review for Solar Photovoltaics. *MRS Energy Sustain.* **2018**, *5*, E13. https://doi.org/10.1557/mre.2018.10.

(9) Foley, S.; Geaney, H.; Bree, G.; Stokes, K.; Connolly, S.; Zaworotko, M. J.; Ryan, K. M. Copper Sulfide (Cu_xS) Nanowire-in-Carbon Composites Formed from Direct Sulfurization of the Metal-Organic Framework HKUST-1 and Their Use as Li-Ion Battery Cathodes. *Adv. Funct. Mater.* **2018**, *28* (19), 1800587. https://doi.org/10.1002/adfm.201800587.

(10) Park, J. Y.; Kim, S. J.; Chang, J. H.; Seo, H. K.; Lee, J. Y.; Yuk, J. M. Atomic Visualization of a Non-Equilibrium Sodiation Pathway in Copper Sulfide. *Nat. Commun.* **2018**, *9*, 922. https://doi.org/10.1038/s41467-018-03322-9.

(11) Jache, B.; Mogwitz, B.; Klein, F.; Adelhelm, P. Copper Sulfides for Rechargeable Lithium Batteries: Linking Cycling Stability to Electrolyte Composition. *J. Power Sources* **2014**, *247*, 703–711. https://doi.org/10.1016/j.jpowsour.2013.08.136.

(12) Raveau, B. Copper Mixed Valence Concept: "Cu(I)–Cu(II)" in Thermoelectric Copper Sulfides—an Alternative to "Cu(II)–Cu(III)" in Superconducting Cuprates. *J. Supercond. Nov. Magn.* **2020**, *33* (1), 259–263. https://doi.org/10.1007/s10948-019-05354-8.

(13) Ohmasa, M.; Suzuki, M.; Takeuchi, Y. A Refinement of the Crystal Structure of Covellite, CuS. *Mineralogical Journal*. **1977**, *8* (6), 311–319.

(14) Suekuni, K.; Tsuruta, K.; Kunii, M.; Nishiate, H.; Nishibori, E.; Maki, S.; Ohta, M.; Yamamoto, A.; Koyano, M. High-Performance Thermoelectric Mineral $Cu_{12-x}Ni_xSb_4S_{13}$ Tetrahedrite. *J. Appl. Phys.* **2013**, *113* (4), 043712. https://doi.org/10.1063/1.4789389.

(15) Suekuni, K.; Tsuruta, K.; Ariga, T.; Koyano, M. Thermoelectric Properties of Mineral Tetrahedrites $Cu_{10}Tr_2Sb_4S_{13}$ with Low Thermal Conductivity. *Appl. Phys. Express* **2012**, *5* (5), 051201. https://doi.org/10.1143/APEX.5.051201.

(16) Lu, X.; Morelli, D. T. Natural Mineral Tetrahedrite as a Direct Source of Thermoelectric Materials. *Phys. Chem. Chem. Phys.* **2013**, *15* (16), 5762–5766. https://doi.org/10.1039/c3cp50920f.

(17) Lu, X.; Morelli, D. T.; Xia, Y.; Zhou, F.; Ozolins, V.; Chi, H.; Zhou, X.; Uher, C. High Performance Thermoelectricity in Earth-Abundant Compounds Based on Natural Mineral Tetrahedrites. *Adv. Energy Mater.* **2013**, *3* (3), 342–348. https://doi.org/10.1002/aenm.201200650.

(18) Suekuni, K.; Kim, F. S.; Takabatake, T. Tunable Electronic Properties and Low Thermal Conductivity in Synthetic Colusites $Cu_{26-x}Zn_xV_2M_6S_{32}$ ($x \leq 4$, M = Ge, Sn). *J. Appl. Phys.* **2014**, *116* (6), 063706. https://doi.org/10.1063/1.4892593.

(19) Suekuni, K.; Kim, F. S.; Nishiate, H.; Ohta, M.; Tanaka, H. I.; Takabatake, T. High-Performance Thermoelectric Minerals: Colusites $Cu_{26}V_2M_6S_{32}$ (M = Ge, Sn). *Appl. Phys. Lett.* **2014**, *105* (13), 132107–132110. https://doi.org/10.1063/1.4896998.

(20) Guélou, G.; Lemoine, P.; Raveau, B.; Guilmeau, E. Recent Developments in High-Performance Thermoelectric Sulphides: An Overview of the Promising Synthetic Colusites. *J. Mater. Chem. C* **2021**, *9* (3), 773–795. https://doi.org/10.1039/d0tc05086e.

(21) Bourgès Yohan; Supka, Andrew; Orabi, Rabih Al Rahal Al; Lemoine, Pierric; Lebedev, Oleg I.; Ohta, Michihiro; Suekuni, Koichiro; Nassif, Vivian; Hardy, Vincent; Daou, Ramzy; Miyazaki, Yuzuru; Fornari, Marco; Guilmeau, Emmanuel, C. B. High-Performance Thermoelectric Bulk Colusite by Process Controlled Structural Disordering. *J. Am. Chem. Soc.* **2018**, *140* (6), 2186–2195.

https://doi.org/10.1021/jacs.7b11224.

(22) Hagiwara, T.; Suekuni, K.; Lemoine, P.; Supka, A. R.; Chetty, R.; Guilmeau, E.; Raveau, B.; Fornari, M.; Ohta, M.; Al Rahal Al Orabi, R.; Saito, H.; Hashikuni, K.; Ohtaki, M. Key Role of d^0 and d^{10} Cations for the Design of Semiconducting Colusites: Large Thermoelectric ZT in $Cu_{26}Ti_2Sb_6S_{32}$ Compounds. *Chem. Mater.* **2021**, *33* (9), 3449–3456. https://doi.org/10.1021/acs.chemmater.1c00872.

(23) Pavan Kumar, V.; Supka, A. R.; Lemoine, P.; Lebedev, O. I.; Raveau, B.; Suekuni, K.; Nassif, V.; Al Rahal Al Orabi, R.; Fornari, M.; Guilmeau, E. High Power Factors of Thermoelectric Colusites $Cu_{26}T_2Ge_6S_{32}$ (T = Cr, Mo, W): Toward Functionalization of the Conductive "Cu–S" Network. *Adv. Energy Mater.* **2019**, *9* (6), 1803249. https://doi.org/10.1002/aenm.201803249.

(24) Pavan Kumar, V.; Guélou, G.; Lemoine, P.; Raveau, B.; Supka, A. R.; Al Rahal Al Orabi, R.; Fornari, M.; Suekuni, K.; Guilmeau, E. Copper-Rich Thermoelectric Sulfides: Size-Mismatch Effect and Chemical Disorder in the $[TS_4]Cu_6$ Complexes of $Cu_{26}T_2Ge_6S_{32}$ (T = Cr, Mo, W) Colusites. *Angew. Chemie Int. Ed.* **2019**, *58* (43), 15455–15463. https://doi.org/10.1002/anie.201908579.

(25) Candolfi, C.; Guélou, G.; Bourgès, C.; Supka, A. R.; Al Rahal Al Orabi, R.; Fornari, M.; Malaman, B.; Le Caër, G.; Lemoine, P.; Hardy, V.; Zanotti, J. M.; Chetty, R.; Ohta, M.; Suekuni, K.; Guilmeau, E. Disorder-Driven Glasslike Thermal Conductivity in Colusite $Cu_{26}V_2Sn_6S_{32}$ Investigated by Mössbauer Spectroscopy and Inelastic Neutron Scattering Christophe. *Phys. Rev. Mater.* **2020**, *4* (2), 25404. https://doi.org/10.1103/PhysRevMaterials.4.025404.

(26) Lai, W.; Wang, Y.; Morelli, D. T.; Lu, X. From Bonding Asymmetry to Anharmonic Rattling in $Cu_{12}Sb_4S_{13}$ Tetrahedrites: When Lone-Pair Electrons Are Not so Lonely. *Adv. Funct. Mater.* **2015**, *25* (24), 3648–3657. https://doi.org/10.1002/adfm.201500766.

(27) Long, S. O.; Powell, A. V.; Hull, S.; Orlandi, F.; Tang, C. C.; Supka, A. R.; Fornari, M.; Vaqueiro, P. Jahn–Teller Driven Electronic Instability in Thermoelectric Tetrahedrite. *Adv. Funct. Mater.* **2020**, *30* (12), 1909409. https://doi.org/10.1002/adfm.201909409.

(28) Shen Yi; Yang, Chun-Chuen; Zhang, Zhao; Li, Shulong; Tung, Yung-Hsiang; Benton,

Allen; Zhang, Xiao; Lu, Xu; Wang, Guoyu; He, Jian; Zhou, Xiaoyuan, X. X. High Thermoelectric Performance in Sulfide-Type Argyrodites Compound $Ag_8Sn(S_{1-x}Se_x)_6$ Enabled by Ultralow Lattice Thermal Conductivity and Extended Cubic Phase Regime. *Adv. Funct. Mater.* **2020**, *30* (21), 2000526. https://doi.org/10.1002/adfm.202000526.

(29) Mukherjee, S.; Voneshen, D. J.; Duff, A.; Goddard, P.; Powell, A. V; Mukherjee, S.; Powell, A. V; Vaqueiro, P. Beyond Rattling: Tetrahedrites as Incipient Ionic Conductors. *Adv. Mater.* **2023**, *35* (44), 2306088. https://doi.org/10.1002/adma.202306088.

(30) Kanishcheva, A. S.; Mikhailov, Y. N.; Trippel, A. F. Refinement of the Crystal Structure of Synthetic Bismuthinite. *Inorg. Mater.* **1981**, *17*, 1466–1468.

(31) Wei, K.; Hobbis, D.; Wang, H.; Nolas, G. S. Wittichenite Cu_3BiS_3: Synthesis and Physical Properties. *J. Electron. Mater.* **2018**, *47* (4), 2374–2377. https://doi.org/10.1007/s11664-017-6053-0.

(32) Adeyemi, A. N.; Clemente, M.; Lee, S. J.; Mantravadi, A.; Zaikina, J. V. Deep Eutectic Solvent-Assisted Microwave Synthesis of Thermoelectric $AgBiS_2$ and Cu_3BiS_3. *ACS Appl. Energy Mater.* **2022**, *5*, 14858−14868. https://doi.org/10.1021/acsaem.2c02336.

(33) Jia, F.; Zhao, S.; Wu, J.; Chen, L.; Liu, T.-H.; Wu, L.-M. Cu_3BiS_3: Two-Dimensional Coordination Induces Out-of-Plane Phonon Scattering Enabling Ultralow Thermal Conductivity. *Angew. Chemie Int. Ed.* **2023**, *e202315642*. https://doi.org/10.1002/anie.202315642.

(34) Kumar, M.; Persson, C. Cu_3BiS_3 as a Potential Photovoltaic Absorber with High Optical Efficiency. *Appl. Phys. Lett.* **2013**, *102* (6), 062109. https://doi.org/10.1063/1.4792751.

(35) Gerein, N. J.; Haber, J. A. One-Step Synthesis and Optical and Electrical Properties of Thin Film Cu_3BiS_3 for Use as a Solar Absorber in Photovoltaic Devices. *Chem. Mater.* **2006**, *18* (26), 6297–6630. https://doi.org/10.1109/WCPEC.2006.279518.

(36) Mesa, F.; Gordillo, G.; Dittrich, T.; Ellmer, K.; Baier, R.; Sadewasser, S. Transient Surface Photovoltage of *p*-Type Cu_3BiS_3. *Appl. Phys. Lett.* **2010**, *96* (8), 082113. https://doi.org/10.1063/1.3334728.

(37) Sun, F. H.; Wu, C. F.; Li, Z.; Pan, Y.; Asfandiyar; Dong, J.; Li, J. F. Powder

Metallurgically Synthesized $Cu_{12}Sb_4S_{13}$ Tetrahedrites: Phase Transition and High Thermoelectricity. *RSC Adv.* **2017**, *7* (31), 18909–18916. https://doi.org/10.1039/c7ra02564e.

(38) Chetty, R.; Bali, A.; Mallik, R. C. Tetrahedrites as Thermoelectric Materials: An Overview. *J. Mater. Chem. C* **2015**, *3* (48), 12364–12378. https://doi.org/10.1039/c5tc02537k.

(39) Bourgès, C.; Lemoine, P.; Lebedev, O. I.; Daou, R.; Hardy, V.; Malaman, B.; Guilmeau, E. Low Thermal Conductivity in Ternary $Cu_4Sn_7S_{16}$ Compound. *Acta Mater.* **2015**, *97*, 180–190. https://doi.org/10.1016/j.actamat.2015.06.046.

(40) Tanishita, T.; Suekuni, K.; Nishiate, H.; Lee, C. H.; Ohtaki, M. A Strategy for Boosting Thermoelectric Performance of Famatinite Cu_3SbS_4. *Phys. Chem. Chem. Phys.* **2020**, *22* (4), 2081–2086. https://doi.org/10.1039/C9CP06233E.

(41) Pfitzner, A.; Bernert, T. The System Cu_3AsS_4-Cu_3SbS_4 and Investigations on Normal Tetrahedral Structures. *Z. Kristallogr. Cryst. Mater.* **2004**, *219* (1), 20–26. https://doi.org/10.1524/zkri.219.1.20.25398.

(42) Berger, L. I.; Prochukhan, V. D. *Ternary Diamond-Like Semiconductors*; *Springer Consultants Bureau, N. Y. C.* **1969**, p. 46.

(43) Tan, G.; Hao, S.; Zhao, J.; Wolverton, C.; Kanatzidis, M. G. High Thermoelectric Performance in Electron-Doped $AgBi_3S_5$ with Ultralow Thermal Conductivity. *J. Am. Chem. Soc.* **2017**, *139* (18), 6467–6473. https://doi.org/10.1021/jacs.7b02399.

(44) Du, B.; Zhang, R.; Chen, K.; Mahajan, A.; Reece, M. J. The Impact of Lone-Pair Electrons on the Lattice Thermal Conductivity of the Thermoelectric Compound $CuSbS_2$. *J. Mater. Chem. A* **2017**, *5* (7), 3249–3259. https://doi.org/10.1039/c6ta10420g.

(45) Kyono, A.; Kimata, M. Crystal Structures of Chalcostibite ($CuSbS_2$) and Emplectite ($CuBiS_2$): Structural Relationship of Stereochemical Activity between Chalcostibite and Emplectite. *Am. Mineral.* **2005**, *90*, 162–165. https://doi.org/10.2138/am.2005.1585.

(46) Tang, Y. Q.; Ge, Z. H.; Feng, J. Synthesis and Thermoelectric Properties of Copper Sulfides via Solution Phase Methods and Spark Plasma Sintering. *Crystals* **2017**, *7* (5),

141. https://doi.org/10.3390/cryst7050141.

(47) Evans, H. T. The Crystal Structures of Low Chalcocite and Djurleite. *Z. Kristallogr. Cryst. Mater.* **1979**, *150*, 299–320. https://doi.org/10.1524/zkri.1979.150.1-4.299.

(48) Kocman, V.; Nuffield, E. W. The Crystal Structure of Cu_3BiS_3. *Acta Crystallogr. Sect. B* **1973**, *29* (11), 2528–2535. https://doi.org/10.1016/j.ssc.2010.01.002.

(49) Portheine, J. C.; Nowachi, W. Refinement of the Crystal Structure of Emplectite, $CuBiS_2$. *Zeitschrift fiir Krist.* **1975**, *141*, 387–402. https://doi.org/10.1038/197070a0.

(50) Bindi, L.; Makovicky, E.; Nestola, F.; De Battisti, L. Sinnerite, $Cu_6As_4S_9$, from the Lengenbach Quarry, Binn Valley, Switzerland: Description and Re-Investigation of the Crystal Structure. *Can. Mineral.* **2013**, *51* (6), 851–860. https://doi.org/10.3749/canmin.51.6.851.

(51) Pauling, L.; Neuman, E. W. The Crystal Structure of Binnite, $(Cu,Fe)_{12}$ As_4S_{13}, and the Chemical Composition and Structure of Minerals of the 1 Etrahedrite Group. *Z. Kristallogr. Cryst. Mater.* **1934**, *88* (1-6), 54–62.

(52) Yaroslavzev, A. A.; Mironov, A. V.; Kuznetsov, A. N.; Dudka, A. P.; Khrykina, O. N. Tennantite: Multi-Temperature Crystal Structure, Phase Transition and Electronic Structure of Synthetic $Cu_{12}As_4S_{13}$. *Acta Crystallogr. Sect. B Struct. Sci. Cryst. Eng. Mater.* **2019**, *75*, 634–642. https://doi.org/10.1107/S2052520619007595.

(53) Wuensch, B. J. The Crystal Structure of Tetrahedrite, $Cu_{12}Sb_4S_{13}$. *Z. Kristallogr. Cryst. Mater.* **1964**, *119*, 453–453. https://doi.org/10.1524/zkri.1964.119.16.437.

(54) Pfitzner, A. Cu_3SbS_3: Zur Kristallstruktur Und Polymorphie. *Z. Anorg. Allg. Chem.* **1994**, *620* (11), 1992–1997. https://doi.org/10.1002/zaac.19946201126.

(55) Pfitzner, A. Disorder of Cu^+ in Cu_3SbS_3: Structural Investigations of the High-and Low-Temperature Modification. *Z. Kristallogr. Cryst. Mater.* **1998**, *213* (4), 228–236. https://doi.org/10.1524/zkri.1998.213.4.228.

(56) Hofmann, W. Strukturelle Und Morphologische Zusammenhänge Bei Erzen Vom Formeltyp ABC_2. *Z. Kristallogr. Cryst. Mater.* **1933**, *84*, 177–203. https://doi.org/10.1524/zkri.1933.84.1.177.

(57) Razmara, M. F.; Henderson, C. M. B.; Pattrick, R. A. D.; Bell, A. M. T.; Charnock, J.

M. The Crystal Chemistry of the Solid Solution Series between Chalcostibite ($CuSbS_2$) and Emplectite ($CuBiS_2$). *Mineral. Mag.* **1997**, *61* (404), 79–88. https://doi.org/10.1180/minmag.1997.061.404.08.

(58) Takéuchi, Y.; Ozawa, T. The Structure of $Cu_4Bi_4S_9$ and Its Relation to the Structures of Covellite, CuS and Bismuthinite, Bi_2S_3. *Z. Kristallogr. Cryst. Mater.* **1975**, *141*, 217–232. https://doi.org/10.1524/zkri.1975.141.3-4.217.

(59) Bente, K.; Kupcik, V. Redetermination and Refinement of the Structure of Tetrabismuth Tetracopper Enneasulphide, $Cu_4Bi_4S_9$. *Acta Crystallogr.* **1984**, *40* (12), 1985–1986. https://doi.org/10.1107/s0108270184010337.

(60) Jiang, Y.; Jia, F.; Chen, L.; Wu, L. M. $Cu_4Bi_4Se_9$: A Thermoelectric Symphony of Rattling, Anharmonic Lone-Pair, and Structural Complexity. *ACS Appl. Mater. Interfaces* **2019**, *11* (40), 36616–36625. https://doi.org/10.1021/acsami.9b11115.

(61) Du, B.; Zhang, R.; Liu, M.; Chen, K.; Zhang, H.; Reece, M. J. Crystal Structure and Improved Thermoelectric Performance of Iron Stabilized Cubic Cu_3SbS_3 Compound. *J. Mater. Chem. C* **2019**, *7* (2), 394–404. https://doi.org/10.1039/c8tc05301d.

(62) Zhu, C.; Ming, H.; Zhang, J.; Li, D.; Chen, T.; Qin, X. Ultralow Lattice Thermal Conductivity and High Thermoelectric Figure of Merit in Dually Substituted $Cu_{12}Sb_4S_{13}$ Tetrahedrites. *Adv. Electron. Mater.* **2022**, *8* (10), 2200110. https://doi.org/10.1002/aelm.202200110.

(63) Chakoumakos, B. C.; Sales, B. C.; Mandrus, D. G.; Nolas, G. S. Structural Disorder and Thermal Conductivity of the Semiconducting Clathrate $Sr_8Ga_{16}Ge_{30}$. *J. Alloys Compd.* **2000**, *296* (1–2), 80–86. https://doi.org/10.1016/S0925-8388(99)00531-9.

(64) Al Rahal Al Orabi, R.; Gougeon, P.; Gall, P.; Al Rahal Al Orabi, R.; Boucher, B.; Fontaine, B.; Gautier, R.; Dauscher, A.; Candolfi, C.; Lenoir, B. X-ray Characterization, Electronic Band Structure, and Thermoelectric Properties of the Cluster Compound $Ag_2Tl_2Mo_9Se_{11}$. *Inorg. Chem.* **2014**, *53* (21), 11699−11709. https://doi.org/10.1021/acs.inorgchem.8b03452.

(65) Jemetio, J. P. F.; Zhou, P.; Kleinke, H. Crystal Structure, Electronic Structure and Thermoelectric Properties of $Cu_4Sn_7S_{16}$. *J. Alloys Compd.* **2006**, *417* (1–2), 55–59. https://doi.org/10.1016/j.jallcom.2005.09.030.

(66) Lemoine, P.; Bourgès, C.; Barbier, T.; Nassif, V.; Cordier, S.; Guilmeau, E. High Temperature Neutron Powder Diffraction Study of the $Cu_{12}Sb_4S_{13}$ and $Cu_4Sn_7S_{16}$ Phases. *J. Solid State Chem.* **2017**, *247*, 83–89. https://doi.org/10.1016/j.jssc.2017.01.003.

(67) Maji, K.; Lemoine, P.; Renaud, A.; Zhang, B.; Zhou, X.; Carnevali, V.; Candolfi, C.; Raveau, B.; Al Rahal Al Orabi, R.; Fornari, M.; Vaqueiro, P.; Pasturel, M.; Prestipino, C.; Guilmeau, E. A Tunable Structural Family with Ultralow Thermal Conductivity: Copper-Deficient $Cu_{1-x}\square_xPb_{1-x}Bi_{1+x}S_3$. *J. Am. Chem. Soc.* **2022**, *144* (4), 1846–1860. https://doi.org/10.1021/jacs.1c11998.

(68) Chen, X.; Shi, L.; Zhou, J.; Goodenough, J. B. Effects of Ball Milling on Microstructures and Thermoelectric Properties of Higher Manganese Silicides. *J. Alloys Compd.* **2015**, *641*, 30–36. https://doi.org/10.1016/j.jallcom.2015.04.048.

(69) Li, M.; Liu, Y.; Zhang, Y.; Han, X.; Zhang, T.; Zuo, Y.; Xie, C.; Xiao, K.; Arbiol, J.; Llorca, J.; Ibáñez, M.; Liu, J.; Cabot, A. Effect of the Annealing Atmosphere on Crystal Phase and Thermoelectric Properties of Copper Sulfide. *ACS Nano* **2021**, *15* (3), 4967–4978. https://doi.org/10.1021/acsnano.0c09866.

(70) Lemoine, P.; Guélou, G.; Raveau, B.; Guilmeau, E. Crystal Structure Classification of Copper-Based Sulfides as a Tool for the Design of Inorganic Functional Materials. *Angew. Chemie Int. Ed.* **2022**, *61* (2), e202108686. https://doi.org/10.1002/anie.202108686.

(71) Kumar, V. P.; Lemoine, P.; Carnevali, V.; Lebedev, O. I.; Boullay, P.; Raveau, B.; Al, R.; Al, R.; Fornari, M.; Prestipino, C.; Menut, D.; Candol, C.; Malaman, B.; Guilmeau, E. Ordered Sphalerite Derivative $Cu_5Sn_2S_7$: A Degenerate Semiconductor with High Carrier Mobility in the Cu–Sn–S Diagram. *J. Mater. Chem. A* **2021**, *9* (17), 10812–10826. https://doi.org/10.1039/d1ta01615f.

(72) Kumar, V. P.; Lemoine, P.; Carnevali, V.; Guélou, G.; Lebedev, O. I.; Raveau, B.; Al Rahal Al Orabi, R.; Fornari, M.; Candolfi, C.; Prestipino, C.; Menut, D.; Malaman, B.; Juraszek, J.; Suekuni, K.; Guilmeau, E. Local-Disorder-Induced Low Thermal Conductivity in Degenerate Semiconductor $Cu_{22}Sn_{10}S_{32}$. *Inorg. Chem.* **2021**, *60* (21), 16273–16285. https://doi.org/10.1021/acs.inorgchem.1c02105.

(73) Chen, K.; Di Paola, C.; Du, B.; Zhang, R.; Laricchia, S.; Bonini, N.; Weber, C.;

Abrahams, I.; Yan, H.; Reece, M. Enhanced Thermoelectric Performance of Sn-Doped Cu_3SbS_4. *J. Mater. Chem. C* **2018**, *6* (31), 8546–8552. https://doi.org/10.1039/c8tc02481b.

(74) Deng, T.; Qiu, P.; Song, Q.; Chen, H.; Wei, T. R.; Xi, L.; Shi, X.; Chen, L. Thermoelectric Properties of Non-Stoichiometric $Cu_{2+x}Sn_{1-x}S_3$ Compounds. *J. Appl. Phys.* **2019**, *126* (8), 085111. https://doi.org/10.1063/1.5115195.

(75) Jiang, Q.; Yan, H.; Lin, Y.; Shen, Y.; Yang, J.; Reece, M. J. Colossal Thermoelectric Enhancement in $Cu_{2+x}Zn_{1-x}SnS_4$ Solid Solution by Local Disordering of Crystal Lattice and Multi-Scale Defect Engineering. *J. Mater. Chem. A* **2020**, *8* (21), 10909–10916. https://doi.org/10.1039/d0ta01595d.

(76) Goto, Y.; Naito, F.; Sato, R.; Yoshiyasu, K.; Itoh, T.; Kamihara, Y.; Matoba, M. Enhanced Thermoelectric Figure of Merit in Stannite–Kuramite Solid Solutions $Cu_{2+x}Fe_{1-x}SnS_{4-y}$ (x = 0–1) with Anisotropy Lowering. *Inorg. Chem.* **2013**, *52*, 9861–9866.

(77) Howard T. Evans, J. Djurleite ($Cu_{1.94}S$) and Low Chalcocite (Cu_2S): New Crystal Structure Studies. *Science.* **1979**, *203* (4378), 356.

(78) Zhu, C.; Chen, Q.; Ming, H.; Qin, X.; Yang, Y.; Zhang, J.; Peng, D.; Chen, T.; Li, D.; Kawazoe, Y. Improved Thermoelectric Performance of $Cu_{12}Sb_4S_{13}$ through Gd-Substitution Induced Enhancement of Electronic Density of States and Phonon Scattering. *ACS Appl. Mater. Interfaces* **2021**, *13*, 25092−25101. https://doi.org/10.1021/acsami.1c03493.

(79) Makovicky, E. The Phase Transformations and Thermal Expansion of the Solid Electrolyte Cu_3BiS_3 between 25 and 300°C. *J. Solid State Chem.* **1983**, *49* (1), 85–92. https://doi.org/10.1016/0022-4596(83)90219-0.

(80) Mizota, T.; Inoue, A.; Yamada, T.; Nakatsuka, A.; Nakayama, N. Ionic Conduction and Thermal Nature of Synthetic Cu_3BiS_3. *Mineralogical Journal*. **1998**, *20* (2), 81–90. https://doi.org/10.2465/minerj.20.81.

(81) Guélou, G.; Pavan Kumar, V.; Carnevali, V.; Lebedev, O. I.; Raveau, B.; Couder, C.; Prestipino, C.; Lemoine, P.; Malaman, B.; Juraszek, J.; Candolfi, C.; Lenoir, B.; Al Rahal Al Orabi, R.; Fornari, M.; Guilmeau, E. Long-Range Cationic Order Collapse Triggered by S/Cl Mixed-Anion Occupancy Yields Enhanced Thermoelectric

Properties in $Cu_5Sn_2S_7$. *Chem. Mater.* **2021**, *33* (23), 9425–9438. https://doi.org/10.1021/acs.chemmater.1c03434.

(82) Liu, H.; Yang, J.; Shi, X.; Danilkin, S. A.; Yu, D.; Wang, C.; Zhang, W.; Chen, L. Reduction of Thermal Conductivity by Low Energy Multi-Einstein Optic Modes. *J. Mater.* **2016**, *2*, 187–195. https://doi.org/10.1016/j.jmat.2016.05.006.

(83) Carnevali, V.; Mukherjee, S.; Voneshen, D. J.; Maji, K.; Guilmeau, E.; Powell, A. V.; Vaqueiro, P.; Fornari, M. Lone Pair Rotation and Bond Heterogeneity Leading to Ultralow Thermal Conductivity in Aikinite. *J. Am. Chem. Soc.* **2023**, *145* (16), 9313–9325. https://doi.org/10.1021/jacs.3c02536.

(84) Cahill, D. G.; Watson, S. K.; Pohl, R. O. Lower Limit to the Thermal Conductivity of Disordered Crystals. *Phys. Rev.* **1992**, *46* (10), 6131–6140.

(85) He, J.; Xia, Y.; Lin, W.; Pal, K.; Zhu, Y.; Kanatzidis, M. G.; Wolverton, C. Accelerated Discovery and Design of Ultralow Lattice Thermal Conductivity Materials Using Chemical Bonding Principles. *Adv. Funct. Mater.* **2022**, *32* (14), 2108532. https://doi.org/10.1002/adfm.202108532.

(86) Das, A.; Pal, K.; Acharyya, P.; Das, S.; Maji, K.; Biswas, K. Strong Antibonding I (p)-Cu (d) States Lead to Intrinsically Low Thermal Conductivity in $CuBiI_4$. *J. Am. Chem. Soc.* **2023**, *145* (2), 1349–1358. https://doi.org/10.1021/jacs.2c11908.

(87) Dutta Shidaling; Prasad, Matukumilli V. D.; Pandey, Juhi; Warankar, Avinash; Mandal, Pankaj; Soni, Ajay; Waghmare, Umesh V.; Biswas, Kanishka, M. M. Ultralow Thermal Conductivity in Chain Like TlSe Due to Inherent Tl^+ Rattling. *J. Am. Chem. Soc.* **2019**, *141* (51), 20293–20299. https://doi.org/10.1021/jacs.9b10551.

(88) Jana, M. K.; Pal, K.; Warankar, A.; Mandal, P.; Waghmare, U. V.; Biswas, K. Intrinsic Rattler-Induced Low Thermal Conductivity in Zintl Type $TlInTe_2$. *J. Am. Chem. Soc.* **2017**, *139* (12), 4350–4353. https://doi.org/10.1021/jacs.7b01434.

(89) Mukhopadhyay, S.; Parker, D. S.; Sales, B. C.; Puretzky, A. A.; McGuire, M. A.; Lindsay, L. Two-Channel Model for Ultralow Thermal Conductivity of Crystalline Tl_3VSe_4. *Science.* **2018**, *360* (6396), 1455–1458. https://doi.org/10.1126/science.aar8072.

(90) Skoug, E. J.; Cain, J. D.; Morelli, D. T. Structural Effects on the Lattice Thermal

Conductivity of Ternary Antimony- and Bismuth-Containing Chalcogenide Semiconductors. *Appl. Phys. Lett.* **2010**, *96* (18), 181905. https://doi.org/10.1063/1.3425886.

(91) Acharyya, P.; Ghosh, T.; Pal, K.; Rana, K. S.; Dutta, M.; Swain, D.; Etter, M.; Soni, A.; Waghmare, U. V.; Biswas, K. Glassy Thermal Conductivity in $Cs_3Bi_2I_6Cl_3$ Single Crystal. *Nat. Commun.* **2022**, *13* (1), 5053. https://doi.org/10.1038/s41467-022-32773-4.

(92) Bouyrie, Y.; Candolfi, C.; Pailhès, S.; Koza, M. M.; Malaman, B.; Dauscher, A.; Tobola, J.; Boisron, O.; Saviot, L.; Lenoir, B. From Crystal to Glass-like Thermal Conductivity in Crystalline Minerals. *Phys. Chem. Chem. Phys.* **2015**, *17* (30), 19751–19758. https://doi.org/10.1039/c5cp02900g.

(93) Christensen, S.; Schmøkel, M. S.; Borup, K. A.; Madsen, G. K. H.; Mcintyre, G. J.; Capelli, S. C.; Christensen, M.; Iversen, B. B. "Glass-like" Thermal Conductivity Gradually Induced in Thermoelectric $Sr_8Ga_{16}Ge_{30}$ Clathrate by off-Centered Guest Atoms. *J. Appl. Phys.* **2016**, *119* (18), 185102. https://doi.org/10.1063/1.4948334.

(94) Nielsen, M. D.; Ozolins, V.; Heremans, J. P. Lone Pair Electrons Minimize Lattice Thermal Conductivity. *Energy Environ. Sci.* **2013**, *6* (2), 570–578. https://doi.org/10.1039/c2ee23391f.

(95) Coughlan, C.; Ibáñez, M.; Dobrozhan, O.; Singh, A.; Cabot, A.; Ryan, K. M. Compound Copper Chalcogenide Nanocrystals. *Chem. Rev.* **2017**, *117* (9), 5865–6109. https://doi.org/10.1021/acs.chemrev.6b00376.

(96) Qiu, W.; Xi, L.; Wei, P.; Ke, X.; Yang, J.; Zhang, W. Part-Crystalline Part-Liquid State and Rattling-like Thermal Damping in Materials with Chemical-Bond Hierarchy. *Proc. Natl. Acad. Sci. U. S. A.* **2014**, *111* (42), 15031–15035. https://doi.org/10.1073/pnas.1410349111.

(97) Suekuni, K.; Lee, C. H.; Tanaka, H. I.; Nishibori, E.; Nakamura, A.; Kasai, H.; Mori, H.; Usui, H.; Ochi, M.; Hasegawa, T.; Nakamura, M.; Ohira-Kawamura, S.; Kikuchi, T.; Kaneko, K.; Nishiate, H.; Hashikuni, K.; Kosaka, Y.; Kuroki, K.; Takabatake, T. Retreat from Stress: Rattling in a Planar Coordination. *Adv. Mater.* **2018**, *30* (13), 1706230. https://doi.org/10.1002/adma.201706230.

(98) Skoug, E. J.; Morelli, D. T. Role of Lone-Pair Electrons in Producing Minimum

Thermal Conductivity in Nitrogen-Group Chalcogenide Compounds. *Phys. Rev. Lett.* **2011**, *107* (23), 235901. https://doi.org/10.1103/PhysRevLett.107.235901.

(99) Li, Z.; Zhou, Z.; Zhang, J.; Zhu, C.; Qiu, P.; Deng, T.; Xu, F.; Chen, L.; Shi, X. Intrinsically Low Thermal Conductivity in a Novel Cu-S Modified ZrS_2 Compound with Asymmetric Bonding. *Small* **2023**, *19* (52), 2304718. https://doi.org/10.1002/smll.202304718.

Table of Content